

# Machine learning-based design of porous graphene with low thermal conductivity

Jing Wan <sup>a</sup>, Jin-Wu Jiang <sup>a,\*</sup>, Harold S. Park <sup>b</sup>

<sup>a</sup> Shanghai Key Laboratory of Mechanics in Energy Engineering, Shanghai Institute of Applied Mathematics and Mechanics, School of Mechanics and Engineering Science, Shanghai University, Shanghai, 200072, People's Republic of China

<sup>b</sup> Department of Mechanical Engineering, Boston University, Boston, MA, 02215, USA

## ARTICLE INFO

### Article history:

Received 10 August 2019

Received in revised form

8 October 2019

Accepted 16 October 2019

Available online 22 October 2019

## ABSTRACT

The thermal conductivity of two-dimensional materials like graphene can efficiently be tuned by introducing holes, in which the density and distribution of the holes are the key parameters. Furthermore, the distribution of holes can induce a variation as high as 74% in the thermal conductivity for porous graphene with a given density of holes. Therefore, an existing challenge is to find the optimal distribution of holes that can minimize or maximize the thermal conductivity of porous graphene as the design space expands dramatically with increasing hole density. We therefore apply an inverse design methodology based on machine learning to reveal the relationship between hole distribution and thermal conductivity reduction in monolayer graphene. The methodology reveals that holes that are randomly distributed transverse to the direction of heat flow, but that exhibit some periodicity along the direction of heat flow, represent the optimal distribution to minimizing the thermal conductivity for porous graphene. Lattice dynamics calculations and wave packet simulations reveal that this spatial distribution effectively causes localization of the phonon modes in porous graphene, which reduces the thermal conductivity. Overall, this work demonstrates the power of machine learning-based design approaches to efficiently obtain new physical insights for scientific problems of interest.

© 2019 Elsevier Ltd. All rights reserved.

## 1. Introduction

Graphene has attracted enormous attention over the past decade due to its excellent physical properties [1]. However, pristine graphene is gapless which limits its application towards graphene-based semiconducting devices. To overcome this drawback, nano-scale holes have been generated in graphene to open a finite bandgap [2]. These holes not only modulate the electronic properties, but also have a significant effect on the thermal transport of graphene. For example, a recent experiment has shown that the thermal conductivity of porous graphene (with controllable number of holes) is considerably lower than that of pristine graphene [3]. Developing approaches to reducing the thermal conductivity is critical for various applications, in particular for high figure of merit thermoelectric materials and devices [4–8].

Theoretical results also show that the thermal conductivity of porous graphene is significantly lower than pristine graphene.

\* Corresponding author.

E-mail address: [jwjiang5918@hotmail.com](mailto:jwjiang5918@hotmail.com) (J.-W. Jiang).

These results show that besides the density of holes, the spatial distribution of the holes also plays an important role in reducing the thermal conductivity. Most works have considered either random or periodic distributions of holes. For instance, several works have examined how to reduce the thermal conductivity by introducing periodic holes [9,10], while Hu et al. found that the thermal conductivity of porous graphene is significantly reduced by randomly distributed holes [11]. Thus, most works have focused on the effect of a specific hole distribution type on the thermal conductivity of graphene. However, determining the optimal hole distribution for maximizing or minimizing the thermal conductivity remains an open question, in particular because the design space increases dramatically with increasing number of holes.

The machine learning (ML) method is a promising tool to screen over a large design space, which has primarily been used to predict properties of new materials [12–18]. However, recent works have begun to use ML to design functional materials and structures while accounting for a potentially large design space. For instance, ML was applied in designing efficient molecular organic light-emitting diodes [19], solid electrolyte in lithium battery [20], composites with high toughness [21], and graphene kirigami with

high yield strain [22]. The ML approach has also been used in predicting the thermal conductivity for nanomaterials and composite materials [23,24]. Based on the ML approach, specific structures have been designed to achieve optimal thermal conductivity for composite materials [25], polymers [26], or nanostructures [27]. Recently, Yamawaki et al. applied the ML approach to search the optimal distribution of holes in the graphene nanoribbons to obtain low thermal conductivity and high thermoelectricity [28], where the holes are one-dimensionally distributed and the effect of two-dimensional distribution of holes in the graphene on the thermal conductivity is still unknown.

In this paper, we study the effect of the density and two-dimensional distribution of holes on the thermal conductivity of porous graphene by combining molecular dynamics (MD) simulations, ML, and lattice dynamics calculations. We set up a convolutional neural network (CNN) model to learn and predict the thermal conductivity of porous graphene, and then perform inverse design to screen millions of candidates to determine the optimal design of porous graphene that exhibits the lowest thermal conductivity, which is a desirable property for thermoelectric materials and devices. The inverse design method based on the ML scheme is able to explore the relationship between the distribution of the holes and the thermal conductivity for the porous graphene, which requires only  $10^3$  simulations out of the full design space of  $10^6$ . The methodology reveals that holes that are randomly distributed transverse to the direction of heat flow, but that exhibit some periodicity along the direction of heat flow, represent the optimal distribution to minimizing the thermal conductivity for porous graphene. Lattice dynamics calculations and wave packet simulations reveal that this spatial distribution effectively localizes the phonon modes in porous graphene, thus reducing the thermal conductivity.

## 2. Thermal conductivity

Fig. 1 shows the structure of porous graphene with dimensions  $160 \times 45$  Å, where the porous region is located at the center of the structure. The atom clusters in blue indicate candidate sites for creating holes, where the size of each hole is about 8.8 Å, which is within the current experimental ability [29]. These atom clusters at the candidate sites can be removed to create holes. For the particular structure in Fig. 1, there are 14 candidate sites, so there are  $2^{14} = 16384$  possible porous structures. The porosity for each structure is defined as the ratio of the number of holes to the total number of candidate sites. It should be noted that the thermal conductivity of graphene depends on the size of the system and the size of the holes [9,10,30]. The present work focuses on exploring the relationship between the distribution of holes and the thermal conductivity of porous graphene, so a fixed size is considered for graphene.

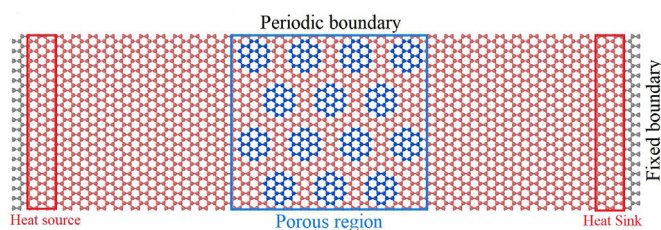


**Fig. 1.** The structure of porous graphene. The left and right ends are fixed during the simulation, while periodic boundary conditions are applied in the vertical direction. Atom clusters (blue online) in the middle region are candidate sites for creating holes. (A colour version of this figure can be viewed online.)

The thermal transport was simulated using non-equilibrium MD, where the temperatures at the heat source and heat sink as shown in Fig. 1 are constant when the system reaches steady state. The structure is divided into 20 sections along the length direction. The first and last sections are fixed during the MD simulations as the adiabatic regions. The thermal energy is pumped into (out) the system in the 2nd (19th) section using the Nosé-Hoover thermostat at temperatures 320 K and 280 K, respectively [31,32], and the other sections are simulated within the NVE ensemble. It should be noted that the Langevin thermostat has been applied in other theoretical studies, as it can also reproduce the canonical ensemble. The properties are statistically indistinguishable from these two thermostats when the system reaches the steady state [33].

The thermal conductivity  $\kappa$  is calculated as follows

$$J = \kappa \frac{(T_{\text{source}} - T_{\text{sink}})}{L_d} \quad (1)$$

where  $J$ ,  $T_{\text{source}}$  and  $T_{\text{sink}}$  are the heat flux, heat source temperature and heat sink temperature in the steady state, respectively and  $L_d$  is the distance between heat source and heat sink. It should be noted that the value of thermal conductivity obtained here is the effective thermal conductivity, which has been used to compare the thermal conductivity for porous materials [34].

All MD simulations were performed using the large-scale atomic molecular massively parallel simulator (LAMMPS) package [35], while the OVITO package is used for visualization [36]. The covalent bonding among carbon atoms is described by the optimized Tersoff potential, which is able to reproduce the experimental value of acoustic-phonon velocities [37]. The standard Newton equations of motion were integrated in time using the velocity Verlet algorithm with a time step of 0.5 fs.

We first show in Fig. 2 the thermal conductivity for all of the 16384 possible porous structures for the graphene shown in Fig. 1. Overall, the thermal conductivity of porous graphene decreases with increasing porosity, but the variation in the thermal conductivity at a given porosity is rather large. For instance, at the porosity of 0.5 (7 holes out of the 14 possible hole sites), the largest and smallest thermal conductivities are  $40 \text{ Wm}^{-1}\text{K}^{-1}$  and  $23 \text{ Wm}^{-1}\text{K}^{-1}$ , respectively; i.e., the variation is as high as 74%. This indicates that the thermal conductivity is strongly dependent on the spatial distribution of the holes, which motivates the present work to design the optimal spatial distribution of the holes such that the thermal conductivity can be maximized or minimized. For the small systems with 14 possible hole sites, we can compute the

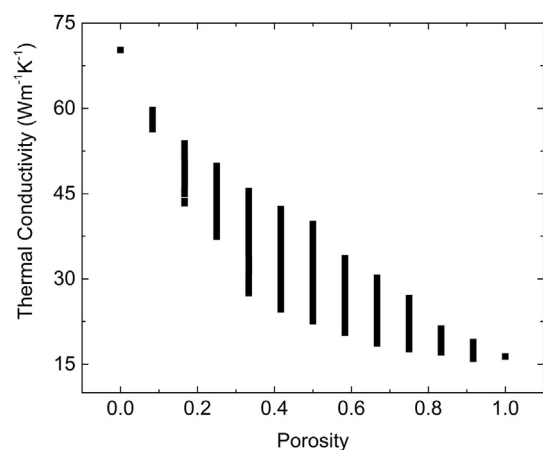


**Fig. 2.** Thermal conductivity versus the density of holes for porous graphene at room temperature.

thermal conductivity for all possible porous structures. However, for larger systems, the number of possible porous structures increases dramatically with increasing site number; it would be impossible to compute the thermal conductivity for all possible porous structures. We will now apply ML to determine the porous structures that exhibit the lowest thermal conductivity.

### 3. Machine learning

#### 3.1. CNN model

In this section, we will train a CNN to predict the thermal conductivity of porous graphene in the context of supervised learning. The architecture of our CNN is inspired by the classic CNN VGGNet [38]. Specifically, the kernel size is  $3 \times 3$  with a stride of 1 in the convolutional (Conv.) layer. Each convolutional layer is followed by a rectified linear unit (ReLU) function and a max-pooling layer of size  $2 \times 2$  with a stride of 2. A fully-connected layer (FCL) is included at the end of model. As a regression problem, the ReLU function will not appear at the final layer. The goal of the parameter optimization is to minimize the root mean square error (RMSE) between the predictions and targets with the Adam optimizer,

$$RMSE = \sqrt{\frac{\sum_{i=1}^{n_t} (y_t^i - y_p^i)^2}{n_t}}, \quad (2)$$

where  $n_t$  is the number of training data, and  $y_t$  and  $y_p$  are the true thermal conductivity obtained from MD simulations and the predicted thermal conductivity by the CNN model, respectively. For a CNN model, we denote 'c' as the number of kernels in a convolutional layer and 'f' as the number of neurons in a FCL. For example, the model CNN-c16c32c64f64 has 16 kernels in first convolutional layer, 32 kernels in second convolutional layer, 64 kernels in third convolutional layer, and 64 neurons in the FCL.

Each training data includes a gray image of size  $54 \times 50$  and its corresponding thermal conductivity value obtained by MD simulations. For the system shown in Fig. 1, there are 16384 training datas, which are divided into three parts: 90% as training set, 5% as validation set, and 5% as test set. The validation is used for hyperparameter tuning to find architecture with optimal performance. The test set is used to estimate the prediction performance of the trained CNN model. In order to evaluate the regression performance of the ML model, we also introduce the following quantity ( $R^2$ ) to measure the quality of the regression performance,

$$R^2 = 1 - \frac{\sum_{i=1}^{n_t} |y_t^i - y_p^i|^2}{\sum_{i=1}^{n_t} |y_t^i - \frac{1}{n_t} \sum_{i=1}^{n_t} y_p^i|^2}. \quad (3)$$

During the tuning, a learning rate of 0.0001 is chosen for the optimizer with a batch size of 200 and the maximum epochs is set to 300. We examine the effects of depth of model and the number of neurons in the FCL on the performance of the CNN. The performance comparison between different models on the validation set is shown in Fig. 3. **Similar to VGGNet, deeper networks perform better than wider networks.** The best model architecture is CNN-c16c32c64f64. The  $R^2$  for model CNN-c16c32c64f64 in the training, validation, and test sets are 0.97, 0.96 and 0.96, respectively. The RMSE for model CNN-c16c32c64f64 in the training, validation, and test sets are 1.22, 1.26 and 1.25, respectively. These results indicate that there is no overfitting for the training process. Fig. 4 shows the performance of the CNN model on the test sets. The RMSE on the test sets is  $1.09 \text{ Wm}^{-1}\text{K}^{-1}$ , which is close to the RMSE

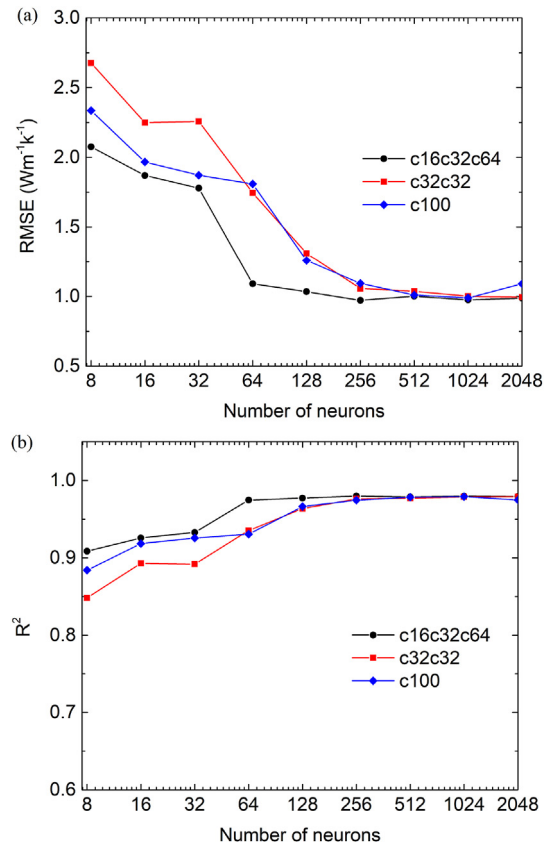


Fig. 3. The performance for the CNN with different hyperparameters: (a) RMSE and (b)  $R^2$ . (A colour version of this figure can be viewed online.)

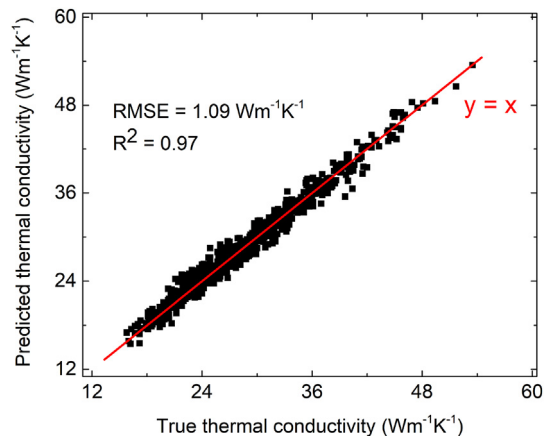


Fig. 4. The fitness in predicted thermal conductivity and true thermal conductivity on the test sets. (A colour version of this figure can be viewed online.)

value ( $0.74 \text{ Wm}^{-1}\text{K}^{-1}$ ) of MD, indicating that the CNN model can accurately predict the thermal conductivity of porous graphene. Note that the RMSE of MD is obtained from the average RMSEs of 5 randomly selected porous structures, and five simulations (with different initial velocity distribution) are performed for each porous structure. The trained model and machine learning code are available in our online repository at <http://jiangjinwu.org>.

#### 3.2. Inverse design

In the previous section, we demonstrated that the CNN can

extract major features of porous graphene and accurately predict the thermal conductivity. Next, we will present an inverse design scheme based on the CNN (CNN-c16c32c64f64) to efficiently search for the porous graphene structure with the lowest thermal conductivity. The ML-based inverse design process we describe here implies that ML can be used to greatly accelerate the search for optimal designs that give a desired property based on a small subset of a much larger design space containing all possible designs [39]. First, we randomly select 100 structures from the library of all possible structures and calculate their thermal conductivity using MD simulations, which are used as training data. Based on these 100 training data, the CNN model is trained as the first generation CNN model. The first generation CNN model is then used to predict the thermal conductivity of all remaining structures in the library, so that another 100 structures with lowest thermal conductivity are predicted. The true thermal conductivity for these 100 new structures are calculated from MD simulations. The data for these 100 new structures are added into the training set, and the enlarged training set is used to train the next generation CNN model. The flow of the search algorithm is shown in Fig. 5. It should be noted that in the design process, the size of the training sets of the CNN model increases gradually with the number of iterations. In each generation of the inverse design process, the CNN model is initialized at first, and then trained based on the training set to predict the thermal conductivity of the remaining structures.

To test the applicability of the search scheme, we consider the smaller system in Fig. 1, which has 14 possible porous sites. We have computed the thermal conductivity for all possible porous structures in Fig. 2, which represents a brute force approach to finding the porous graphene structures with the lowest thermal conductivity. We will show that the above search scheme can efficiently find these porous graphene structures with the lowest thermal conductivity. To evaluate the performance of the search scheme, we use the average thermal conductivity of the top 100 structures with the lowest thermal conductivity in the training sets of each generation as the convergence measurement. As a benchmark, random search approach is introduced for comparison. As shown in Fig. 6, the average thermal conductivity of random search approach converges slowly, and it needs to explore the entire design space to find the optimal structure with the lowest thermal conductivity. In contrast, the search scheme based on the CNN model is able to find the top 5 structures in the 3rd generation (only requires 300 MD simulations), and screen for the top 100 structures in the 7th generation (700 MD simulations). This indicates that the CNN model can effectively find the optimal structures with the lowest

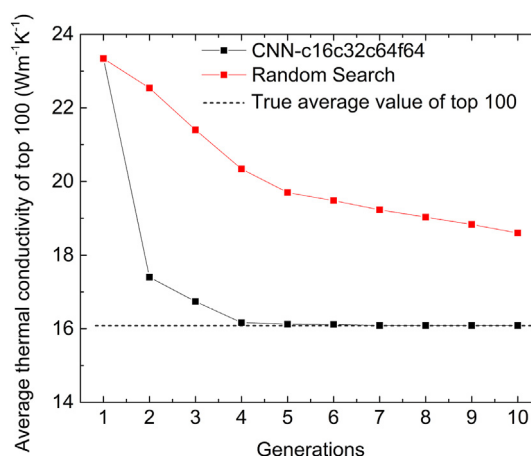


Fig. 6. Average thermal conductivity of top 100 structures in each generation during the inverse design of the smaller system with 14 candidate hole sites. (A colour version of this figure can be viewed online.)

thermal conductivity. In our work, one MD simulation for the smaller graphene system in Fig. 1 takes 2 h of computing time using 4 cores of CPU. Using the CNN model to predict or train the thermal conductivity of one porous structure needs 1 ms computing time using 4 cores of CPU plus one GPU. Therefore, using the CNN model to perform structure design is very effective and fast.

We have demonstrated that the CNN model can be used to effectively find the optimal designs from a small design space (16384) where the thermal conductivity of all possible structures is known. Now we apply the CNN search algorithm to a large design space where the optimal structures are unknown. We consider a longer system with 24 possible porous sites, and focus on these porous structures with porosity of 0.5 (12/24). The entire design space (12/24) has  $24!/(12!12!) = 2704156$  possible structures. We aim to determine the porous structure with the lowest thermal conductivity among this huge number of possible porous structures. An efficient design process is required here due to the inherent challenge in performing such a large number of MD simulations for all possible structures.

The size of the input image is expanded to  $90 \times 50$ , to account for the increase in the length of the porous region, and we include the random search approach for comparison. Fig. 7 shows that the search scheme based on the CNN model is able to find the structures with low thermal conductivity. Specifically, the average thermal conductivity of top 100 structures (containing 12 holes) in the training sets is  $14.99 \text{ Wm}^{-1}\text{K}^{-1}$  for the 8th generation.

In Fig. 8, we plot the top 5 structures with the lowest thermal conductivity for different generations. It can be seen that the distribution of the holes is quite random in the initial stage, but it quickly evolves to some regular distributions, where the holes are separated in columns perpendicular to the direction of heat flow. We also present 3 typical structures and their corresponding thermal conductivity on the right side of Fig. 8. We have thus demonstrated the ability in finding porous structures with lowest thermal conductivity for the search scheme based on the CNN.

## 4. Discussions

### 4.1. Lattice dynamics calculation

The above-discussed CNN-based inverse design method successfully determined porous graphene structures with ultra-low

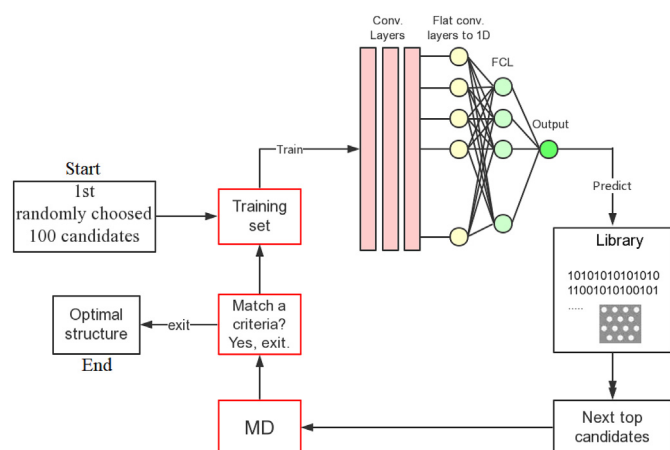
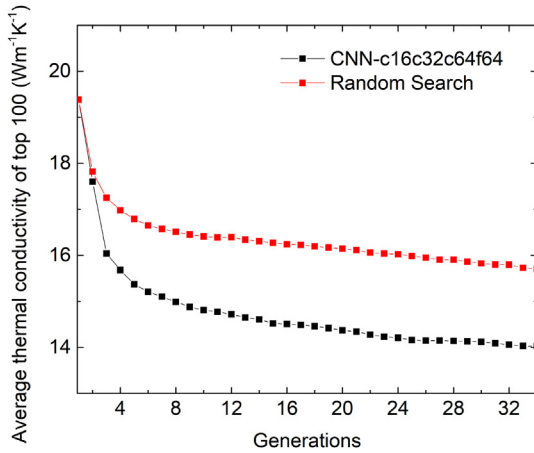
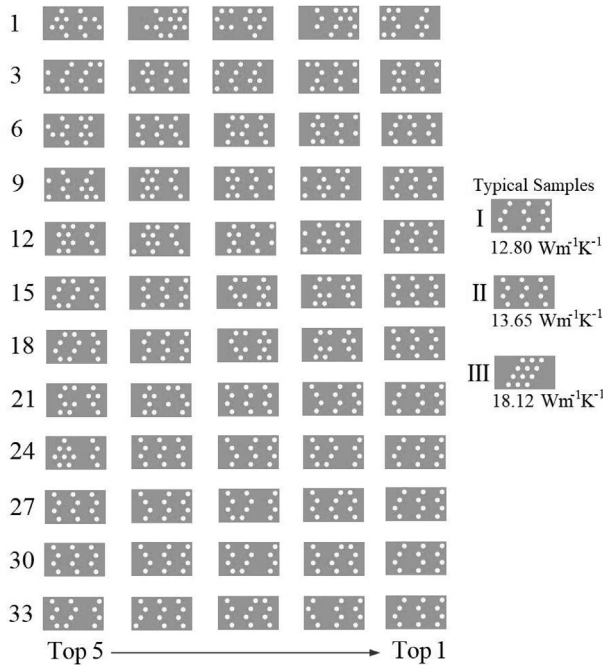


Fig. 5. Schematic of the search algorithm based on the CNN model. (A colour version of this figure can be viewed online.)





**Fig. 7.** Average thermal conductivity of top 100 structures in each generation for the inverse design of porous graphene with 24 candidate hole sites. (A colour version of this figure can be viewed online.)



**Fig. 8.** The porous structure of the top 5 configurations with lowest thermal conductivity found by CNN model. Right: three representative porous structures and their thermal conductivity value.

thermal conductivity. In particular, the first two typical porous structures shown in Fig. 8 have significantly lower thermal conductivity than the third typical structure. The reduction of the thermal conductivity in the porous graphene may be related to the localization property of the defected structure. To investigate the mechanisms underlying the ultra-low thermal conductivity of the porous graphene structure found by the ML approach, we examine the localization of the phonon modes in the porous graphene. We calculated the frequencies and eigenvectors (vibrational morphology) of all phonon modes for these three typical porous structures. The phonon calculations were performed with GULP [40].

The localization of the phonon modes can be evaluated through the inverse participation ratio (IPR), which is defined as follows for phonon mode  $k$ ,

$$P_k^{-1} = \sum_{i=1}^N \left( \sum_{\alpha=1}^3 u_{i\alpha,k}^2 \right)^2, \quad (4)$$

where  $N = 1872$  is the total number of atoms for the porous graphene, and  $u_{i\alpha,k}$  is the  $\alpha$  component of atom  $i$  in the eigenvector of mode  $k$ . According to this definition, a large IPR value represents a localized phonon mode, while a small IPR value corresponds to an extended phonon mode. The phonon mode with a larger IPR value is more strongly localized in space. Fig. 9 compares the IPR for phonon modes in the three typical porous graphene structures. We consider phonon modes with frequency within the range  $[0, 500] \text{ cm}^{-1}$ , as low-frequency phonons are more important for thermal transport than high-frequency phonons. These phonon modes with IPR around 0.01 in Fig. 9 are localized modes, while phonon modes with IPR around 0.001 are extended modes. The IPR for the first two typical structures are overall higher than the third typical structure. More specifically, the averaged value for the IPR of these three typical porous structures are 0.0029, 0.0025, and 0.0022 (solid black lines). The averaged value for the IPR is obviously larger in the first two typical porous structures, which indicates that phonon modes in the first two typical porous structures are overall more localized as compared with the third typical porous structure.

The eigenvectors of three representative localized phonon modes are shown in Fig. 10 (a), (b) and (c) for the three typical porous structures. The representative localized phonon is chosen for each structure to reflect the vibrational component of atoms in the porous area. The arrow attached on each atom represents the atomic vibrational component in the phonon mode. These phonon modes have large IPR value of 0.0125, 0.0111, and 0.0118, so they are localized modes. In these phonon modes, atoms within the porous region have large vibrational component, while other atoms far away from the porous region have almost no vibrational component. In the first two porous structures, the holes are more scattered in the space, so more atoms fall within the porous region. In contrast, for the third typical porous structure, holes are distributed in a rather compact manner, leading to smaller area for the porous region. In other words, the first two typical porous structures have more degrees of freedom in the porous region than the third typical porous structure, so there are more localized phonon modes in the first two typical porous structures. As a result, the effective defected area in the first two porous structures is more effective in localizing thermal energy, which leads to lower thermal conductivity in the first two typical porous structures.

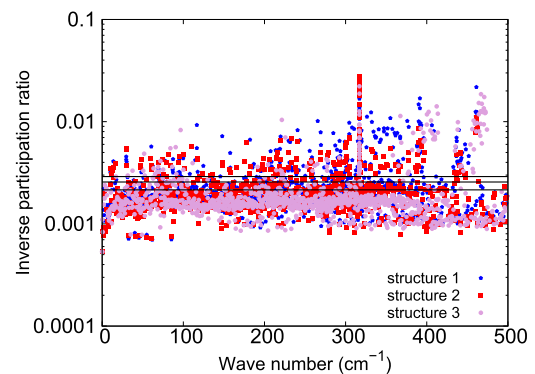


**Fig. 9.** (Color online) The IPR for the three typical structures shown in Fig. 8. The horizontal lines at 0.0029, 0.0025, and 0.0022 are the average value for the IPR for the three typical structures. Note that the averaged IPR for the third structure is obviously smaller than the other two structures. (A colour version of this figure can be viewed online.)

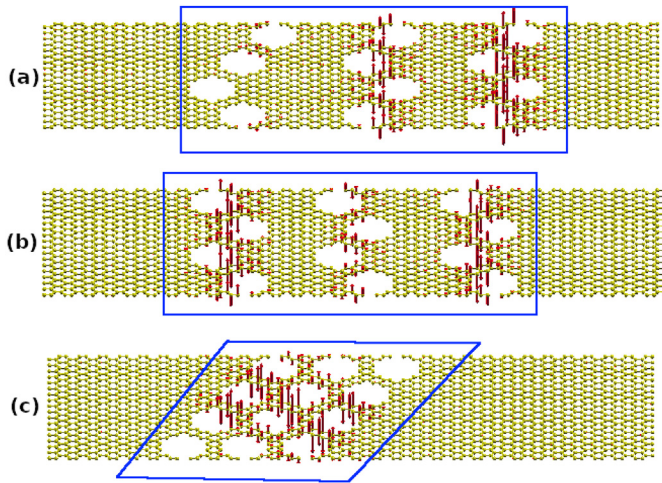


**Fig. 10.** (Color online) Eigenvectors (vibrational morphology) for representative localized phonon modes for the three typical structures shown in Fig. 8. The arrow attached to each atom represents the atomic vibrational component in the phonon mode. (a) Phonon mode with IPR as 0.0125 and frequency  $\omega = 461.5 \text{ cm}^{-1}$  for the first typical structure. (b) Phonon mode with IPR as 0.0111 and frequency  $\omega = 462.5 \text{ cm}^{-1}$  for the second typical structure. (c) Phonon mode with IPR as 0.0118 and frequency  $\omega = 464.2 \text{ cm}^{-1}$  for the third typical structure. Effective porous areas are enclosed by blue boxes. (A colour version of this figure can be viewed online.)

#### 4.2. Wave packet simulation

To further explore the localization effect on the thermal transport, we perform wave packet simulations to investigate the effect of the porous region on the transport of a wave packet. As shown in Fig. 11 (a), the left and right parts of the system are perfect graphene, while the typical porous structure sits in the middle of the whole simulated system as the defected region. The wave packet is created in the left region of the system and travels toward the middle defected region. The middle defected region can be any one of these three typical porous structures shown in Fig. 8. We will

compare the capability of localizing thermal energy for these three typical porous structures.

The wave packet is generated using the frequency and eigenvector of perfect graphene. The base for the primitive unit cell of the honeycomb lattice structure are  $\vec{a}_1 = (\sqrt{3}/2, -1/2, 0)a$  and  $\vec{a}_2 = (\sqrt{3}/2, 1/2, 0)a$ , with  $a = 2.46 \text{ Å}$  as the lattice constant for graphene. The corresponding reciprocal lattice base are  $\vec{b}_1 = (1/2, -\sqrt{3}/2, 0)b$  and  $\vec{b}_2 = (1/2, \sqrt{3}/2, 0)b$ , with  $b = 4\pi/(\sqrt{3}a)$  as the reciprocal lattice constant.

In this set of simulations, the wave packet is constructed based on the phonon mode at  $\vec{k} = 0.1\vec{b}_1 + \vec{b}_2$  with the frequency of  $407.2 \text{ cm}^{-1}$ . The group velocity for this mode is  $254.1 \text{ Å/ps}$  from the lattice dynamics calculation. From Fig. 11 (a), the wave packet travels for a distance of  $264.0 \text{ Å}$  within  $1.21 \text{ ps}$ , so the velocity for the wave packet is about  $218.2 \text{ Å/ps}$ . The velocity for the phonon mode in the wave packet simulation is slightly smaller than that from the lattice dynamics calculation because the system in the wave packet simulation is mechanically deformed due to the relaxation of the defected porous region, resulting in a weak reduction of phonon velocity.

Fig. 11 (b) shows the distribution of the atomic kinetic energy in the first typical structure during the wave packet simulation. The color represents the kinetic energy (in eV) of each atom. At the beginning of the simulation, the wave packet originates in the left side of the structure, so there is no kinetic energy in the defected region. The wave packet arrives at the defected region around  $2.0 \text{ ps}$ . Obvious kinetic energy is localized in the defected region after  $4.0 \text{ ps}$ , which directly reflects the high localization capability for the first typical porous structure. Similar as the first typical porous structure, Fig. 11 (c) shows that obvious atomic kinetic energy is localized at the second typical porous defected region after a long simulation time of  $4.0 \text{ ps}$ . However, Fig. 11 (d) discloses a much weaker localization effect for the third typical porous structure. The kinetic energy localized in the defected region is much smaller than that in the first two typical porous structures. The wave packet simulations thus verifies the lattice dynamics calculations in the previous section. We can thus claim that the first two typical porous

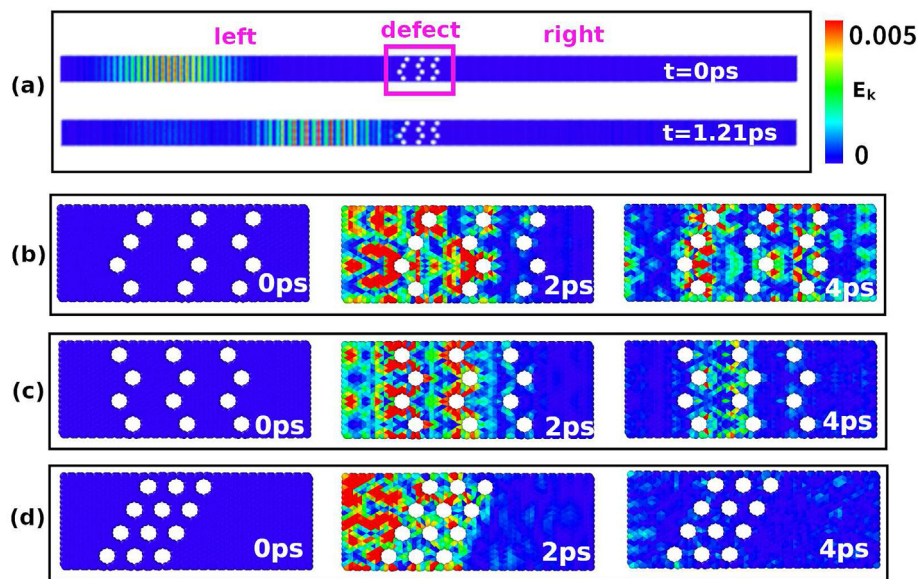


**Fig. 11.** (Color online) Wave packet simulation for porous graphene. (a) The wave packet is created in the left region at time  $0 \text{ ps}$  and travels to the porous region at time  $1.21 \text{ ps}$ . The atomic kinetic energy distribution at time  $0 \text{ ps}$ ,  $2.0 \text{ ps}$ , and  $4.0 \text{ ps}$  for (b) the first typical porous structure, (c) the second typical porous structure, and (d) the third typical porous structure in Fig. 8. Less kinetic energy is localized in the third typical porous structure. The color bar represents the kinetic energy for each atom. (A colour version of this figure can be viewed online.)

structures have larger effective porous area, which results in a stronger localization capability. As a result, the first two typical porous structures have lower thermal conductivity than the third typical porous structure.

Finally, we also note that there is a small difference in the average IPR between the first two porous structures in Fig. 8, which indicates that the phonon modes in the first typical porous structure are more localized than those of the second typical porous structure. This difference is attributed to the different distribution of holes. Furthermore, from the top 5 porous structures explored by generation 33 in Fig. 8 where the holes exhibit some periodicity along the direction of heat flow in all five structures, it can be seen that the specific distribution of holes is another factor to further reduce the thermal conductivity. Thus, not only the effective porous area but also the specific distribution of holes within the area is critical to reducing the thermal conductivity of graphene.

## 5. Conclusion

In conclusion, the density of the holes and the distribution of the holes are both important for controlling the thermal conductivity of porous graphene, as the variation of the thermal conductivity can be as high as 74% for porous structures with the same porosity of 0.5. We have applied an inverse design approach based on a CNN to determine, out of a large ( $10^6$ ) design space, the optimal porous graphene structures that have the lowest thermal conductivity. This ML-based inverse design methodology is highly efficient, as we needed to only simulate about  $10^3$  structures out of the total  $10^6$  possible structures. Furthermore, the ML approach found porous structures that successfully lowered the thermal conductivity by localizing phonon modes within the porous regions within the graphene sheet. This localization mechanism is further verified by lattice dynamics calculations and wave packet simulations. The ML model finds that holes that are randomly distributed transverse to the direction of heat flow, but that exhibit some periodicity along the direction of heat flow, represent the optimal distribution to minimizing the thermal conductivity for porous graphene. Our work shows ML approach is able to effectively find the optimal structures exhibiting the correct physics without any physical insight.

## Declaration of competing interest

The authors declare that they have no known competing financial interests or personal relationships that could have appeared to influence the work reported in this paper.

## Acknowledgment

We thank Paul. Z. Hanakata for his helpful discussion of the CNN model. The work is supported by the National Natural Science Foundation of China (NSFC) under Grant No. 11822206, and the Innovation Program of Shanghai Municipal Education Commission under Grant No. 2017-01-07-00-09-E00019.

## References

- [1] A.K. Geim, Graphene: status and prospects, *Science* 324 (5934) (2009) 1530–1534.
- [2] J. Bai, X. Zhong, S. Jiang, Y. Huang, X. Duan, Graphene nanomesh, *Nat. Nanotechnol.* 5 (3) (2010) 190.
- [3] J. Oh, H. Yoo, J. Choi, J.Y. Kim, D.S. Lee, M.J. Kim, et al., Significantly reduced thermal conductivity and enhanced thermoelectric properties of single- and bi-layer graphene nanomeshes with sub-10 nm neck-width, *Nano Energy* 35 (2017) 26–35.
- [4] H. Sevincli, G. Cuniberti, Enhanced thermoelectric figure of merit in edge-disordered zigzag graphene nanoribbons, *Phys. Rev. B* 81 (11) (2010) 113401.
- [5] F. Mazzamuto, V.H. Nguyen, Y. Apertet, C. Caër, C. Chassat, J. Saint-Martin, et al., Enhanced thermoelectric properties in graphene nanoribbons by resonant tunneling of electrons, *Phys. Rev. B* 83 (23) (2011) 235426.
- [6] L.D. Zhao, S.H. Lo, Y. Zhang, H. Sun, G. Tan, C. Uher, et al., Ultralow thermal conductivity and high thermoelectric figure of merit in snse crystals, *Nature* 508 (7496) (2014) 373.
- [7] Y. Xu, Z. Li, W. Duan, Thermal and thermoelectric properties of graphene, *Small* 10 (11) (2014) 2182–2199.
- [8] S. Bathula, M. Jayasimhadri, B. Gahtori, N.K. Singh, K. Tyagi, A. Srivastava, et al., The role of nanoscale defect features in enhancing the thermoelectric performance of p-type nanostructured sige alloys, *Nanoscale* 7 (29) (2015) 12474–12483.
- [9] L. Yang, J. Chen, N. Yang, B. Li, Significant reduction of graphene thermal conductivity by phononic crystal structure, *Int. J. Heat Mass Transf.* 91 (2015) 428–432.
- [10] M. Yarifard, J. Davoodi, H. Rafii-Tabar, In-plane thermal conductivity of graphene nanomesh: a molecular dynamics study, *Comput. Mater. Sci.* 111 (2016) 247–251.
- [11] S. Hu, Z. Zhang, P. Jiang, J. Chen, S. Volz, M. Nomura, et al., Randomness-induced phonon localization in graphene heat conduction, *J. Phys. Chem. Lett.* 9 (14) (2018) 3959–3968.
- [12] B. Meredig, A. Agrawal, S. Kirklin, J.E. Saal, J. Doak, A. Thompson, et al., Combinatorial screening for new materials in unconstrained composition space with machine learning, *Phys. Rev. B* 89 (9) (2014), 094104.
- [13] K. Schütt, H. Glawe, F. Brockherde, A. Sanna, K. Müller, E. Gross, How to represent crystal structures for machine learning: towards fast prediction of electronic properties, *Phys. Rev. B* 89 (20) (2014) 205118.
- [14] K. Hansen, F. Biegler, R. Ramakrishnan, W. Pronobis, O.A. Von Lilienfeld, K.R. Müller, et al., Machine learning predictions of molecular properties: accurate many-body potentials and nonlocality in chemical space, *J. Phys. Chem. Lett.* 6 (12) (2015) 2326–2331.
- [15] K.T. Butler, D.W. Davies, H. Cartwright, O. Isayev, A. Walsh, Machine learning for molecular and materials science, *Nature* 559 (7715) (2018) 547.
- [16] M.A. Matos, S.T. Pinho, V.L. Tagarielli, Application of machine learning to predict the multi-axial strain-sensing response of cnt-polymer composites, *Carbon* 146 (2019) 265–275.
- [17] Z. Zhang, Y. Hong, B. Hou, Z. Zhang, M. Negahban, J. Zhang, Accelerated discoveries of mechanical properties of graphene using machine learning and high-throughput computation, *Carbon* 148 (2019) 115–123.
- [18] V.Y. Iakovlev, D.V. Krasnikov, E.M. Khabushev, J.V. Kolodiaznaia, A.G. Nasibulin, Artificial neural network for predictive synthesis of single-walled carbon nanotubes by aerosol cvd method, *Carbon* 153 (2019) 100–103.
- [19] R. Gómez-Bombarelli, J. Aguilera-Iparraguirre, T.D. Hirzel, D. Duvenaud, D. Maclaurin, M.A. Blood-Forsythe, et al., Design of efficient molecular organic light-emitting diodes by a high-throughput virtual screening and experimental approach, *Nat. Mater.* 15 (10) (2016) 1120.
- [20] A.D. Sendek, Q. Yang, E.D. Cubuk, K.A.N. Duerloo, Y. Cui, E.J. Reed, Holistic computational structure screening of more than 12000 candidates for solid lithium-ion conductor materials, *Energy Environ. Sci.* 10 (1) (2017) 306–320.
- [21] G.X. Gu, C.T. Chen, M.J. Buehler, De novo composite design based on machine learning algorithm, *Extrem. Mech. Lett.* 18 (2018) 19–28.
- [22] P.Z. Hanakata, E.D. Cubuk, D.K. Campbell, H.S. Park, Accelerated search and design of stretchable graphene kirigami using machine learning, *Phys. Rev. Lett.* 121 (25) (2018) 255304.
- [23] H. Yang, Z. Zhang, J. Zhang, X.C. Zeng, Machine learning and artificial neural network prediction of interfacial thermal resistance between graphene and hexagonal boron nitride, *Nanoscale* 10 (40) (2018) 19092–19099.
- [24] H. Wei, S. Zhao, Q. Rong, H. Bao, Predicting the effective thermal conductivities of composite materials and porous media by machine learning methods, *Int. J. Heat Mass Transf.* 127 (2018) 908–916.
- [25] A. Seko, A. Togo, H. Hayashi, K. Tsuda, L. Chaput, I. Tanaka, Prediction of low-thermal-conductivity compounds with first-principles anharmonic lattice-dynamics calculations and bayesian optimization, *Phys. Rev. Lett.* 115 (20) (2015) 205901.
- [26] S. Wu, Y. Kondo, M.a. Kakimoto, B. Yang, H. Yamada, I. Kuwajima, et al., Machine-learning-assisted discovery of polymers with high thermal conductivity using a molecular design algorithm, *npj Computational Materials* 5 (1) (2019) 5.
- [27] S. Ju, T. Shiga, L. Feng, Z. Hou, K. Tsuda, J. Shiomi, Designing nanostructures for phonon transport via bayesian optimization, *Phys. Rev. X* 7 (2) (2017), 021024.
- [28] M. Yamawaki, M. Ohnishi, S. Ju, J. Shiomi, Multifunctional structural design of graphene thermoelectrics by bayesian optimization, *Sci. Adv.* 4 (6) (2018), eaar4192.
- [29] P. Masih Das, G. Danda, A. Cupo, W.M. Parkin, L. Liang, N. Kharche, et al., Controlled sculpture of black phosphorus nanoribbons, *ACS Nano* 10 (6) (2016) 5687–5695.
- [30] X. Xu, L.F. Pereira, Y. Wang, J. Wu, K. Zhang, X. Zhao, et al., Length-dependent thermal conductivity in suspended single-layer graphene, *Nat. Commun.* 5 (2014) 3689.
- [31] S. Nosé, A unified formulation of the constant temperature molecular dynamics methods, *J. Chem. Phys.* 81 (1) (1984) 511–519.
- [32] W.G. Hoover, Canonical dynamics: equilibrium phase-space distributions, *Phys. Rev. A* 31 (3) (1985) 1695.



- [33] J.E. Basconi, M.R. Shirts, Effects of temperature control algorithms on transport properties and kinetics in molecular dynamics simulations, *J. Chem. Theory Comput.* 9 (7) (2013) 2887–2899.
- [34] M. Wang, J. Wang, N. Pan, S. Chen, Mesoscopic predictions of the effective thermal conductivity for microscale random porous media, *Phys. Rev.* 75 (3) (2007), 036702.
- [35] S. Plimpton, Fast parallel algorithms for short-range molecular dynamics, *J. Comput. Phys.* 117 (1) (1995) 1–19.
- [36] A. Stukowski, Visualization and analysis of atomistic simulation data with ovito—the open visualization tool, *Model. Simul. Mater. Sci. Eng.* 18 (1) (2009), 015012.
- [37] L. Lindsay, D. Broido, Optimized tersoff and brenner empirical potential parameters for lattice dynamics and phonon thermal transport in carbon nanotubes and graphene, *Phys. Rev. B* 81 (20) (2010) 205441.
- [38] K. Simonyan, A. Zisserman, Very Deep Convolutional Networks for Large-Scale Image Recognition, 2014 arXiv preprint arXiv:1409.1556.
- [39] A. Zunger, Inverse design in search of materials with target functionalities, *Nat. Rev. Chem.* 2 (4) (2018), 0121.
- [40] J.D. Gale, Gulp: a computer program for the symmetry-adapted simulation of solids, *J. Chem. Soc., Faraday Trans.* 93 (4) (1997) 629–637.